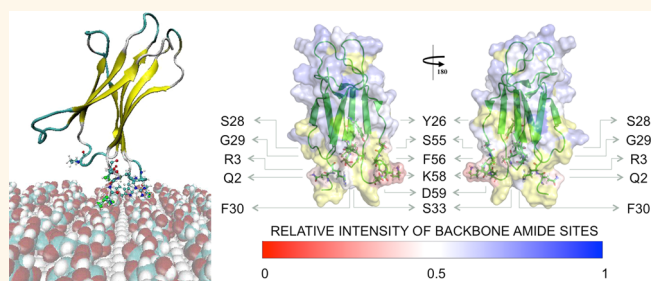


Probing the Influence of Citrate-Capped Gold Nanoparticles on an Amyloidogenic Protein

Giorgia Brancolini,^{*,†} Alessandra Corazza,^{*,§} Marco Vuano,[‡] Federico Fogolari,^{*,§} Maria Chiara Mimmi,[‡] Vittorio Bellotti,^{§,⊥,||} Monica Stoppini,^{§,⊥} Stefano Corni,^{*,†} and Gennaro Esposito^{*,‡,§,||}

[†]Center S3, CNR Institute Nanoscience, Via Campi 213/A, 41125 Modena, Italy, [‡]Dipartimento di Scienze Mediche e Biologiche (DSMB), University of Udine, Piazzale Kolbe 4, 33100 Udine, Italy, [§]Istituto Nazionale Biostrutture e Biosistemi, Viale medaglie d'Oro 305, 00136 Roma, Italy, [⊥]Dipartimento di Medicina Molecolare, Universita' di Pavia, Via Taramelli 3, 27100 Pavia, Italy, ^{||}Division of Medicine, University College of London, London NW3 2PF, U.K., and ^{*}Science and Math Division, New York University at Abu Dhabi, Abu Dhabi, UAE

ABSTRACT Nanoparticles (NPs) are known to exhibit distinct physical and chemical properties compared with the same materials in bulk form. NPs have been repeatedly reported to interact with proteins, and this interaction can be exploited to affect processes undergone by proteins, such as fibrillogenesis. Fibrillation is common to many proteins, and in living organisms, it causes tissue-specific or systemic amyloid diseases. The nature of NPs and their surface chemistry is crucial in assessing their affinity for proteins and their effects on them. Here we present the first detailed structural characterization and molecular mechanics model of the interaction between a fibrillogenic protein, β_2 -microglobulin, and a NP, 5 nm hydrophilic citrate-capped gold nanoparticles. NMR measurements and simulations at multiple levels (enhanced sampling molecular dynamics, Brownian dynamics, and Poisson–Boltzmann electrostatics) explain the origin of the observed protein perturbations mostly localized at the amino-terminal region. Experiments show that the protein–NP interaction is weak in the physiological-like, conditions and do not induce protein fibrillation. Simulations reproduce these findings and reveal instead the role of the citrate in destabilizing the lower pH protonated form of β_2 -microglobulin. The results offer possible strategies for controlling the desired effect of NPs on the conformational changes of the proteins, which have significant roles in the fibrillation process.



KEYWORDS: nanoparticles · amyloid · fibrillogenesis · docking · molecular dynamics · nuclear magnetic resonance

The interaction between proteins and nanoparticles (NPs)^{1–5} is central to many aspects of nanoscience and several nanotechnological applications.⁶ Among these, examples of relevant areas of interest are the nanoparticle-based medical imaging and drug delivery.^{7–10} These applications entail the administration of NPs to living organisms, which raises a number of issues concerning immunology, toxicology, biochemistry, biophysics, etc., often leading to assessment and analysis of NP/protein interaction processes that are central also in nanoscale bioanalytics.^{11,12} The subject of NP/protein interaction has been addressed by several investigators over the past decades, and recent reviews are available to summarize the state-of-the-art technology.^{4,13,14} From a general viewpoint, nanoparticles have been reported to

either affect or leave unchanged protein structure and function, depending on the specific properties of the nanoparticle surface and dimensions, the environmental conditions, and the actual protein characteristics.^{4,14,15} The basic pattern that proteins elicit on interaction with NPs is the formation of tightly and/or loosely bound layers around the NPs. These layers are referred to as corona and represent the very essence of the relationship between the NPs and the surrounding biological environment.¹⁶

Particular relevance has been attributed to the interaction of NPs with amyloidogenic proteins due to the interest in possible therapeutic approaches^{17–20} for a class of pathologies with poor treatment, if any. Most of the available evidence, however, points to an enhanced amyloid fibril formation

* Address correspondence to giorgia.brancolini@nano.cnr.it, stefano.corni@nano.cnr.it, gennaro.esposito@uniud.it.

Received for review October 29, 2014 and accepted February 19, 2015.

Published online February 19, 2015 10.1021/nn506161j

© 2015 American Chemical Society

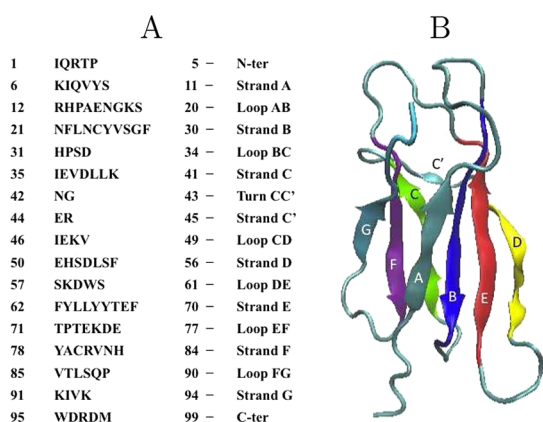


Figure 1. (A) Protein sequence. (B) Tertiary structure and topology of β_2 -microglobulin.

in the presence of NPs.^{19,20} In particular, it was shown²¹ that different types of NPs, such as copolymer particles, cerium oxide particles, quantum dots, and carbon nanotubes, enhance the fibril nucleation rate of β_2 -microglobulin (β_2 m), that is, the light chain of the class I major histocompatibility complex (MHC-I) that is responsible for a tissue-specific amyloidosis in long-term hemodialyzed patients.²² Secondary and tertiary structure and topology of β_2 m are reported in Figure 1.

As β_2 m fibrils did not appear physically linked to any of the NPs accelerating their onset, the faster growth was attributed to increased protein concentration in the vicinity of the NP surface, with a mechanism that had already been proposed to account for the protein tissue-specific deposition in collagen-rich regions.²³ However, a microscopic characterization of the β_2 m–NP interaction is still lacking, preventing a chemical understanding of the mechanisms that govern the fate of the protein. We present here a comprehensive investigation of β_2 m in the presence of citrate-coated gold NPs that, by combining synergically experiments and simulations, unravels such a microscopic picture. Citrate anions reduce gold ions to atoms and stabilize colloidal AuNPs formed from clustered atoms,²⁴ and the so-formed citrate-capped gold nanoparticles (cit-AuNPs) are among the most investigated in this field.^{3,25–28} Despite the large number of experimental investigations exploiting cit-AuNPs, the structural details of citrate anions adsorbed on the AuNP surface are still poorly understood.²⁹ Yet, they certainly constitute an array of negative charges that can interact with proteins. This is particularly relevant for β_2 m because, for its tissue-specific deposition, a mechanism has been proposed based on the effects of the collagen²³ and heparin³⁰ charge arrays in promoting local concentration increase and fibril nucleation.

To advance the understanding of the mechanisms driving the adsorption/deposition of amyloidogenic proteins to charged surfaces and the potential influence on fibrillogenesis, we present a comprehensive study based on the protein structural characterization

by NMR and molecular simulations of the protein/nanoparticle system. Both simulations and experimental results support the conclusions that cit-AuNPs, in the physiological-like experimental conditions probed here, have a quite labile interaction with β_2 m that does not lead to fibrillation. Our combined experimental and simulation approach reveals the protein patch interacting with the NP and suggests that conformational rearrangements associated with protein protonation are accentuated by the interaction with the citrate adlayer.

Not surprisingly, our findings on the NP effects on fibrillation are different from those previously obtained with other NPs and in other environmental conditions on this amyloidogenic protein. The previously reported results²¹ have been paradigmatic and rather influential for most of the successive interpretations, but, as pointed out in a commentary to the original report,³¹ different scenarios can be envisaged because of the enormous variability that is possible for the NP size, shape, surface coating, and composition. By learning how to exploit that variability, we aim at specifically fine-tuning the NP properties to rescue protein fibrillation or revert their amyloid deposition.¹⁸

RESULTS AND DISCUSSION

Docking of β_2 m on Negative Gold. In this section, we investigate the nature of the binding of β_2 m to a citrate-coated gold surface by means of Brownian dynamics (BD) docking.

Among the various crystal surfaces, we have considered the (111) plane (*i.e.*, Au(111)), which is the most stable and the most commonly occurring in nanoparticles.³² In this section, we shall consider extended gold surfaces, larger than the crystal faces that can be found on the experimental 5 nm gold NP. This simplifying assumption might create differences on the extent of the electrostatic interaction felt by the protein. The role of the finite particle size on the electrostatic interaction will be specifically tested by a continuum electrostatic model in the Role of Nanoparticle Actual Size on the Electrostatic Interaction section. Finally, for a surfactant-covered nanoparticle, possibly reactive edges and vertexes are certainly passivated by the surfactant itself.

The nature of the binding of β_2 m to a citrate-coated gold surface, as well as the effect of a negative surface potential, was initially investigated by introducing a small negative charge density per gold surface atom. The charge density of ($\text{Au}_{\text{chg}}^{\text{net}} = -0.05e$) per surface atom used in the calculation was determined by assuming an ordered monolayer of fully deprotonated citrate molecules on gold, as shown in Figure 2. The regular citrate adlayer on the top of Au(111) was generated with a ratio of the surface gold ion and citrate concentrations that was suitable to reproduce experimental electrochemical data on the cit-AuNP

system under aqueous conditions and at physiological pH.^{33,39}

In short, we generated the structures of protein–surface encounter complexes by running Brownian dynamics simulations during which the internal structure of the protein was kept rigid (rigid docking). The interaction (free) energy of the protein with the surface was obtained using the ProMetCS protein–metal continuum solvent model,⁴⁰ and adsorption free energies of β_2m on the Au(111) surface were computed for the structures resulting from the docking. The protein–surface encounter complexes obtained during a BD simulation trajectory were clustered to identify genuinely different protein orientations. For each of the most populated complexes, which were ranked by size, a representative structure was selected.

During docking, the interaction energy of the protein with the Au(111) surface is described by three main terms:⁴⁰ van der Waals energy described by site–site Lennard-Jones, E_{LJ} , interactions; adsorbate–metal electrostatic interaction energy, U_{EP} ; and the desolvation energy of the protein, U_{ds}^p , and of the metal surface, U_{ds}^m (see Table 1). The electrostatic term arises from surface polarization and includes an image-charge term.⁴¹

When this docking procedure was applied to the β_2m –AuNP system with negatively charged gold surface atoms ($Au_{chg}^{net} = -0.05e$), it yielded a single orientation accounting for more than 98% of the total encounter complexes. The representative structure of the resulting complex is shown in Figure 3. The complex stability and the protein residues contacting the surface are listed in Table 1.

The binding in complex A is stabilized mostly by the electrostatic terms. The preferred orientation involves

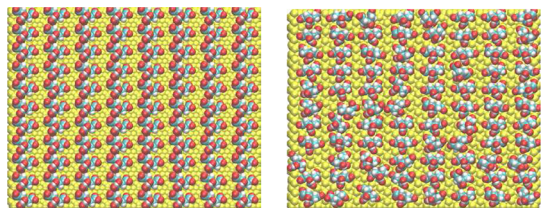


Figure 2. Initial (on the left) and final (on the right) citrate anion distribution on positively charged Au(111) after 20 ns of classical MD with GoIP and OPLS/AA in SPC/E water.

the residues at the N-terminal (ARG3) tail and DE loop (LYS58, ASP59, and TRP60). The strong and highly populated binding seems to be associated with the total charge of the gold surface atoms and the amount of charged residues contacting the surface (see Table 1), and this is due to the fact that in the presence of negatively charged gold the protein is able to use simultaneously more than one charged contact in order to optimize the binding. For completeness, we extended the docking to surfaces with 5-fold lower surface charge density ($Au_{chg}^{net} = -0.01e$). Complex A remains the most populated, but other complexes also appear (results are reported Figure 1 and Table 1 of Supporting Information).

Atomistic Molecular Dynamics (MD) Simulations of β_2m on Citrate-Covered Au. In order to disclose the possible conformational changes induced on the structure of the protein by the adsorption on cit-AuNPs, which may have significant roles in the fibrillation process, the stability of the encounter complexes resulting from the rigid docking was assessed by performing atomistic MD simulations.

As an atomistic molecular mechanics model for cit-AuNPs, we propose a surface in which the fully deprotonated citrate anions ($C_3H_5O(COO)_3^{3-}$) are described as interacting adsorbed species on a positively charged AuNP. For the sake of completeness, we also consider the comparison with a different citrate-covered surface model based on a neutral gold core and the

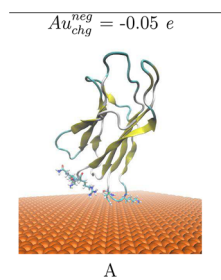


Figure 3. Most populated encounter complex of β_2m on a negatively charged gold nanocluster obtained by BD simulation. For $Au_{chg}^{neg} = -0.05e$, the structure of a single complex is representative for 98% of the total encounter complexes. The protein backbone is shown as cartoon representation. The residues contacting the gold surface are shown in stick representation.

TABLE 1. Resultant Encounter Complex from Rigid-Body BD Docking of β_2m (1JNJ) to a Au(111) Surface^a

label	RelPop % ^b	U_{Repr} ^c	E_{LJ} ^d	$E_{LJ} + U_{ds}^p + U_{ds}^m$ ^e	U_{EP} ^f	spread ^g	contact residues ^h
A	98	−41.380	−44.020	−10.278	−31.100	0.322	ARG3 LYS58 ASP59 TRP60

^a A hierarchical clustering algorithm (based on a minimum distance linkage function) was applied to the diffusional encounter complexes after docking to a bare negative gold ($Au_{chg}^{neg} = -0.05e$) surface. The reported complexes represent 98% of the encounter complexes obtained by BD simulation. ^b Relative population of this cluster. ^c U_{Repr} : Total interaction energy of the representative of the given cluster in kT with $T = 300$ K. ^d E_{LJ} : Lennard-Jones energy term for the representative complex. ^e U_{ds}^p : Nonpolar (hydrophobic) desolvation energy of the representative complex, in kT . ^f U_{EP} : Surface desolvation energy of the representative complex, in kT . ^g U_{EP} : Total electrostatic energy of the representative complex, in kT . ^h Root-mean-square deviation of the structures within the cluster with respect to the representative complex. ⁱ Residues with atoms contacting gold at distances ≤ 3 Å.

counterions included in aqueous solution over the citrate, namely, cit3Na-AuNPs (*i.e.*, three Na^+ ions released from each sodium citrate when it is put in aqueous solution). Simulation results are summarized in the Supporting Information (section Validation of the Au surface with a positive charge density and Figure 3). Such results are qualitatively similar to those presented later in the main text for the positive gold core model, although in somewhat less agreement with NMR data than the main text model. In fact, we believe that the choice of a positive gold core is more in line with current understanding of citrate-covered gold nanoparticles. For instance, in ref 33, the authors reported an open circuit potential for freshly formed colloids (460–560 mV vs SCE), corresponding to a positive gold core for both pH 1 and pH 3 accompanied by a modest tendency of the gold core to be pH-sensitive in passing from pH 1 to pH 3. In our opinion, the latter results support the assumption of a positive gold core even at higher pH. More importantly, in ref 34, a positive gold NP core at pH 7.5 was proposed on the basis of experiments. Additionally, in ref 35, the authors reported a ζ -potential of -40 to -50 mV for 10 nm nanoparticles, in a pH range from 5 to 12. The ionic strength was not clearly reported there, but it was reasonable to assume that it was about 20–30 mM at neutral pH. Based on a Poisson–Boltzmann estimate, this ζ -potential would require a surface charge density of approximately -0.2 e/nm². Such values must be reproduced with a citrate surface concentration, which in previous works was reported to be in the range from 1.4×10^{-10} to 5×10^{-10} mol/cm².^{36,37} Our atomistic model satisfies these experimental constraints, by using a reasonable citrate surface concentration of 2.8×10^{-10} mol/cm² and by including a positive gold core to obtain a surface charge density of -0.3 e/nm².

To our knowledge, the formation of a citrate adlayer composed of interacting citrate molecules as a stabilizing layer has never been incorporated in simulations involving proteins due to the lack of suitable force fields (FFs) able to describe the citrate anion, as well as their interfacial physisorption on the top of the gold nanoparticle. Such FFs were developed only recently.³⁸

At first, the stability of the citrate adlayer on the top of Au(111) in aqueous solution was assessed by using 20 ns of standard MD simulations at 300 K. The initial and final distributions of the citrate anion on the positively charged AuNP are shown in Figure 2. None of the citrate was displaced from the surface during the entire length of the simulation in explicit water, in line with experimental knowledge. The distribution of citrate was stabilized on the top of the AuNP surface by direct contact with the surface gold atoms, and no large distortion of the adlayer from the initial conformation has been observed.

In order to enhance the effective sampling space of our protein–cit–AuNP system, we have applied REMD

involving multiple independent simulations at different temperatures (T-REMD). In the present simulation protocol, the system periodically attempts an exchange in temperature space,^{42,43} thus enabling replicas at low temperature to exchange to a higher temperature where energy barriers may be more easily crossed. In this way, we overcome the limit of straight MD simulations which are known to suffer from the quasi-ergodic problem; that is, simulations at low temperature tend to get trapped in a local minimum energy state.⁴²

Given the experimental evidence demonstrating that the neutral nonprotonated wild-type $\beta_2\text{m}$ does not form amyloid fibrils *in vitro*,^{44–46} we have generated the effect of both nonprotonating and protonating conditions by using two fully solvated systems, which were equilibrated under constant temperature for 20 ns with standard MD: (i) nonprotonated normal $\beta_2\text{m}$ (PDB code 1JNJ, *i.e.*, with only HIS51 and HIS84 protonated); (ii) protonated normal $\beta_2\text{m}$ (PDB code 1JNJ with also HIS31 protonated). The present experimental pH conditions are correctly described by a nonprotonated regime for the protein, but given the presence of the negative citrate adlayer which may stabilize the protonated regime, both regimes may be relevant and should be investigated. The comparison of the two protonation states is very important here because the protonation state has been found to be relevant in determining the stability of the protein and of the barrier crossing energies between the normal and amyloidogenic form of βm .^{47–51} For example, a very low pH was used in ref 21, at which HIS31 is certainly protonated.

Before starting the T-REMD, we applied to both systems an equilibration protocol which consists of various steps of optimization of atomic coordinates and restrained finite-temperature dynamics during which the restraints on protein atoms were gradually weakened and eventually released, according to a previously reported procedure.^{52–54} At the end of the equilibration, the trajectories were stable in terms of density, temperature, potential energy, and other macroscopic properties. The equilibration phases of the nonprotonated and protonated protein were followed by 20 ns of unrestrained T-REMD in which 32 replicas on the top of the cit–Au(111) surface for each system were used, yielding an aggregated simulation time of 640 ns. During the 20 ns of T-REMD, the proteins of each replica were fully flexible and the water molecules, ions, and citrates were treated explicitly in the simulations.

Simulation results are summarized in Figure 4 in which panel (a) refers to nonprotonated protein and panel (b) refers to protonated protein.

The top panel of Figure 4a shows the final representative structures of the two most recurrent orientations found for the nonprotonated protein, and

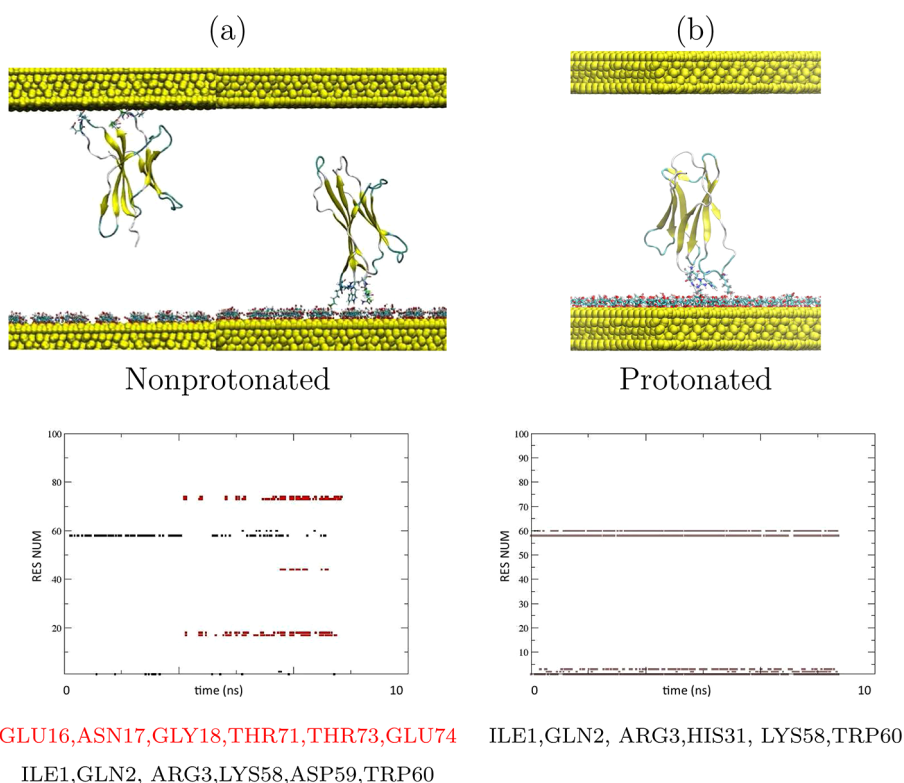


Figure 4. (a) Nonprotonated protein and (b) protonated protein. Top panel (a) shows the most representative structures of the nonprotonated protein during T-REMD, and top panel (b) shows the orientation for the protonated protein on cit-AuNPs. In both cases, the results are obtained following the replica at the lowest temperature during 20 ns of T-REMD. Bottom panels (a,b) report the time evolution of contacting residues (*i.e.*, residues with atoms within 0.6 nm from the Au surface) for the nonprotonated (in red for the upper orientation and in black for the lower orientation, respectively) and protonated (in brown) protein with respect to the surface of the nanoparticle, extracted from the last 10 ns of the total 20 ns T-REMD.

Figure 4b shows the unique stable orientation for the protonated protein. In both cases, the results were obtained following the replica at the lowest temperature during the 20 ns of T-REMD. The bottom panels of Figure 4a,b report the time evolution of contacting residues for the nonprotonated (a) and protonated (b) protein with respect to the surface of the nanoparticle, along the last 10 ns of T-REMD. In the case of the nonprotonated protein, the patch contacting the citrate surface is not conserved during the simulation, which points to a loosely bound neutral protein on the top of cit-AuNPs. On the contrary, for the protonated protein (Figure 4b), the contact patch is unique and well conserved during the entire 20 ns length of T-REMD since the protein is never able to detach from the citrate layer during the 20 ns but it remains anchored through the N-terminal residues (ILE1, GLN2, ARG3) and DE loop residues (LYS58, TRP60). The capability of the nonprotonated protein to detach from the citrate surface during T-REMD is in line with the labile, transient interaction measured by the experiments (as will be discussed in the next sections).

The structural impact on (i) nonprotonated and (ii) protonated proteins upon adsorption on the top of the cit-Au(111) surface was analyzed with an additional conformational analysis (sorting and averaging of the

trajectories) of the simulated systems to select a few representative structures of the proteins contacting the cit-Au(111) through the N-terminal tail. Clustering with a simple means algorithm was applied during the last 5 ns of the 20 ns T-REMD, extracting (i) one relevant representative structure for the nonprotonated protein and (ii) six relevant representative structures for the protonated protein (shown in Figure 5) covering the 50% of the total population in both cases.

The unique nonprotonated structure has a root-mean-square deviation (rmsd) value of 1.96 Å with respect to the NMR reference structure (PDB code 1JNJ), pointing to modest internal rearrangements of the nonprotonated protein. On the contrary, protonated structures have rmsd with respect to NMR reference (PDB code 1JNJ modified by protonation of HIS31 residue) ranging from 2.15 to 3.45 Å, referring to local rearrangements of loops AB, DE, BC, and strand D (see Figure 5). In all cases, the internal rearrangements of the proteins suggest the absence of unfolding events in the short term that are able to destructure the secondary structure of the native protein. However, the larger rmsd and the larger variety of structures observed for the protonated protein point to a lower stability of the system under acidic conditions upon adsorption on cit-Au. Moreover, a deeper analysis

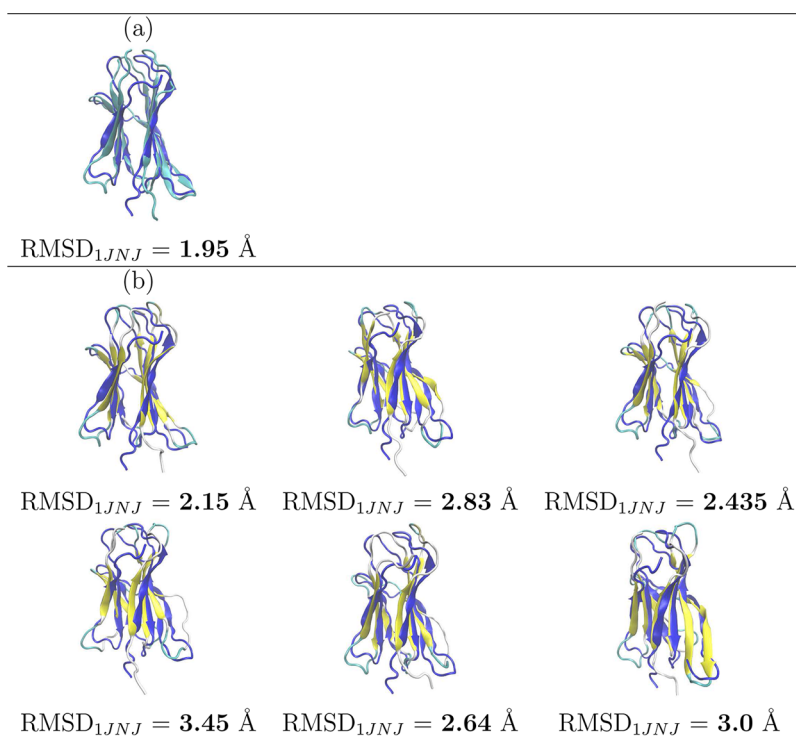


Figure 5. Cluster analysis of the conformational rearrangements of the protein on cit-AuNPs during the last 5 ns of the 20 ns of T-REMD following replica at the lowest temperature and computed rmsd with respect to the NMR reference structure. (a) Nonprotonated protein and (b) protonated protein. Resulting structures cover 50% of the total population in both cases.

showed that, among the structures with the largest rmsd with respect to the NMR reference, the largest deviations were localized at the BC loop region, which belongs to the hydrophobic pocket formed by the N-terminus, BC and FG loop, as discussed in ref 47. To quantify, the rmsd values restricted to the atoms of the BC loop (residues 31–34) were evaluated and found to range from (i) 2.5 Å for the nonprotonated case to (ii) 3.4 Å for the protonated case, with respect to the NMR reference. For the sake of comparison, the same rmsd values restricted to the BC loop (for the nonprotonated β_2m) were compared with that of the same protein interacting with a hydrophobic nanoparticle ($\text{Au}_{25}\text{L}_{18}^-$, $\text{L} = \text{S}(\text{CH}_2)_2\text{Ph}$) through the same hydrophobic patch.⁵⁵ In that case, the rmsd value was only 1.6 Å. The reported behavior points to an induced larger exposure of the protonated HIS31 side chains upon adsorption to hydrophilic surfaces with respect to hydrophobic surfaces. The native *cis*-prolyl peptide bond (between HIS31 and PRO32) switches to *trans* as part of the transition to the amyloidogenic state. It is well-known that the conversion of the HIS31–PRO32 peptide bond from *cis* to *trans* requires the breaking of a network of hydrogen bonds⁵⁶ and of the interactions stabilizing the hydrophobic pocket.⁴⁷ This transition may therefore be catalyzed by the interactions of N-terminal residues with the adlayer of citrate. We were not able to observe the *cis*–*trans* transition in our simulations, due to the low probability of the event and the length of the simulations. To understand if the

citrate adlayer has a role in the conformational rearrangements of the protonated protein, we have repeated the same 20 ns T-REMD simulation for the protein in bulk solution (same number of replicas). Focusing on the BC loop, we observed a decrease in the rmsd from 3.4 Å on cit-AuNP to 2.2 Å in solution for the protonated case (the rmsd of the entire protein also decreased). These findings indicate that the citrate adlayer magnifies the conformational changes related to protein protonation. To investigate this point further, we additionally performed configurational principal component analysis to reveal the structures underlying the atomic fluctuations and the region of the protein with the highest degree of correlation, which may be directly connected through bonds or move in a concerted manner. In Figure 6, we report a direct comparison between the first three dominant fluctuations of the (i) nonprotonated and (ii) protonated protein in solvent and upon interaction with the cit-AuNPs. In the case of (i) nonprotonated protein, the largest collective motions of atoms are localized at the N-terminal tail and DE loop regions, whereas in the (ii) protonated case, fluctuations of the BC loop, involving the HIS31–PRO32 peptide bond, are more relevant especially in the vicinity of the adlayer of citrate (see modes 1 and 2 in Figure 6) and appear to be slightly correlated to the fluctuation of the proximal DE loop belonging to the same hydrophobic pocket. More in detail, fluctuations at the BC loop appear to be larger when fluctuations at the DE loop are larger. On the

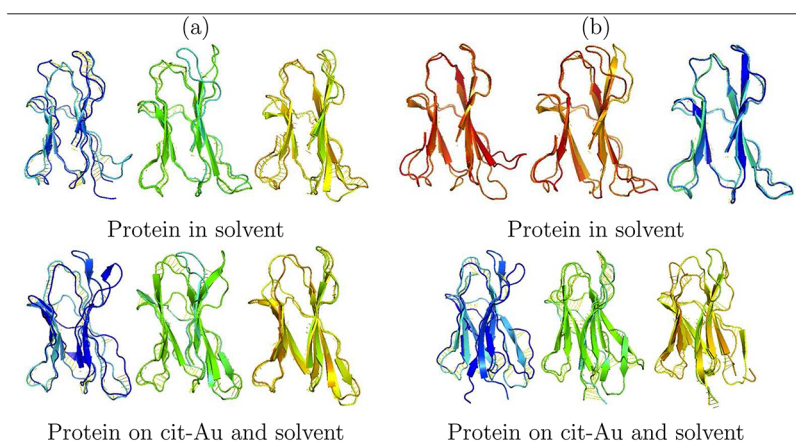


Figure 6. Principal component analysis: direct comparison between the first three dominant fluctuations of the (a) nonprotonated protein and (b) protonated protein in solvent and upon interaction with the cit-AuNPs. Protonated and nonprotonated proteins in solvent exhibit very similar dynamics, while the protonated protein on the surface has distortions notably larger than that of the nonprotonated one.

contrary, fluctuations at the BC and DE loop appear to be larger when fluctuations at the AB loop are smaller and *vice versa*. The comparison clearly shows the role of the interaction with the charged surface of cit-AuNPs on the induced conformational changes of the protonated protein, which are absent in water and much more limited for the nonprotonated case.

To summarize, with a number of T-REMD refining runs, we were able to assess the global stability of complex A already predicted by rigid-body BD docking on the top of negatively charged AuNPs. The protein was always contacting the nanoparticle through the apical region representing the edges of the D and E β -strand and N-terminal tail. The protonated and nonprotonated forms of the proteins showed quite different stability when interacting with the citrate layer (largest changes and fluctuations for the protonated). In particular, the comparison between the protonated β_2m behavior in solution and interacting with the citrates suggests that the latter accentuate the structural destabilization following protonation.

Role of Nanoparticle Actual Size on the Electrostatic Interaction. In order to support the assumption based on a flat surface, the nanoparticle coated by citrate was additionally simulated by a dielectric sphere with a diameter of 5 nm (as in the experiments) and with the same density of negative charge as in the Brownian dynamics model ($-1.38 e/nm^2$).

Because the goal of this model was to test the effect of finite particle size on electrostatic characteristics, only electrostatic interactions were considered. It was also assumed, based on explicit computations for a few randomly selected rotamers, that the generalized Born radii of the atoms are not changed significantly by the presence of the nanoparticle, as long as the two systems remain well separated.

Generalized Born radii have been computed according to the GBR6 model, which was shown to be

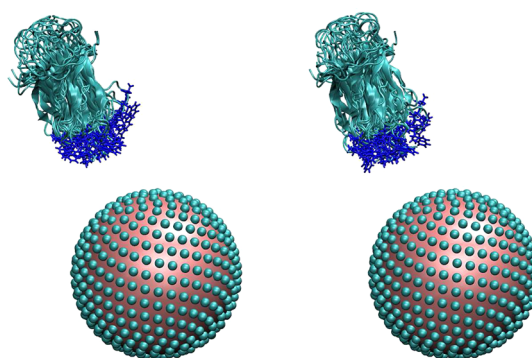


Figure 7. Ten lowest energy arrangements of β_2 -microglobulin (shown together) and a model of a citrate-coated nanoparticle for the neutral protein (left panel) and positively charged protein (right panel). Citrate moieties are modeled as 3 Å spheres on the surface of a 25 Å sphere representing the nanoparticle. The side chains of residues 1, 3, 31, 59, and 60 of the protein are shown in blue.

extremely accurate for proteins.⁵⁷ The set of 10 rotamers leading to the system's lowest electrostatic energy are superimposed and displayed in Figure 7 for the neutral and positively charged states of β_2 -microglobulin.

The number of favorable orientations and the computed interaction energies depend on the distance between the centers of mass, on the radius assumed for the citrate particles, and on the charge state of the protein. For the neutral state, there are 384 favorably interacting orientations out of 800, whereas for the positively charged state, the same figure rises to 425. Notwithstanding these differences, it is seen that for all orientations the N-terminal region is pointing toward the negative nanoparticle. The same conclusion holds for all of the possible 16 protonation states of the four histidines, although the number of favorably interacting orientations and the interaction energy depend on the histidines' protonation state (data not shown).

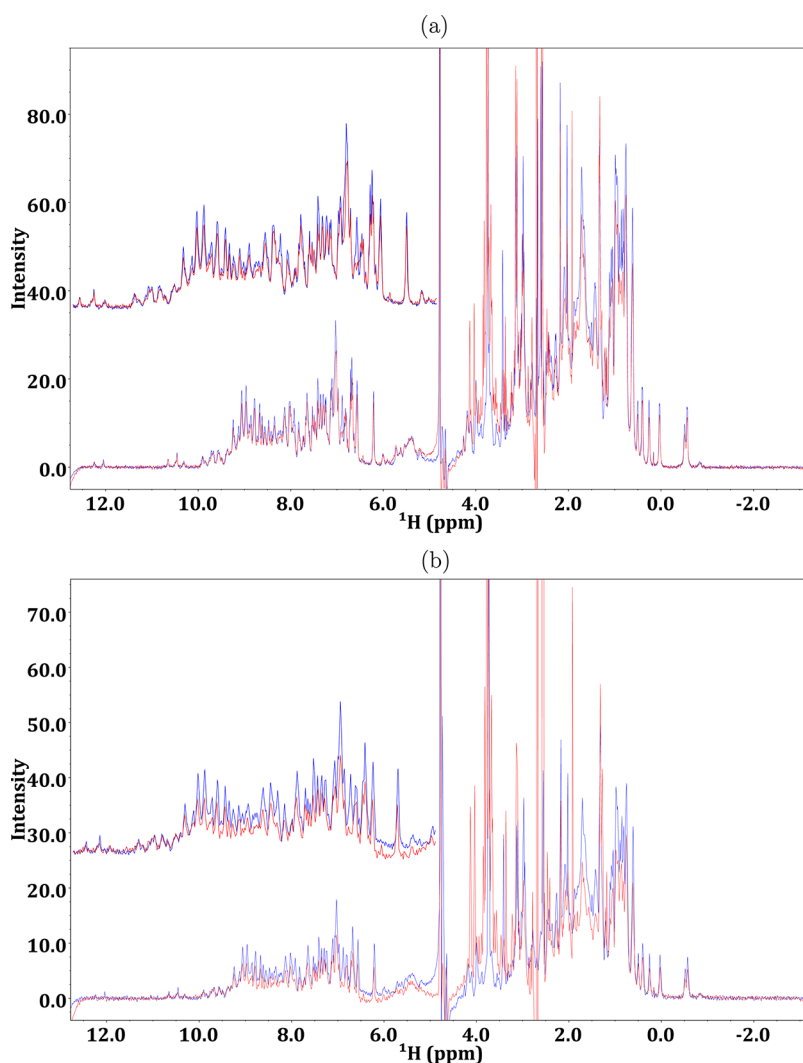


Figure 8. One-dimensional ^1H NMR spectra: In blue and red are the traces of the protein alone and in the presence of gold nanoparticles at 130 nM, pH 6.47, and 298 K. The protein concentration is 36 and 17 μM in (a) and (b), respectively. A few limited changes are seen upon adding Au nanoparticles. Among these, we can identify shifts of the phenyl hydrogens of F56 around 6.5 and 6.9 ppm (the corresponding amide resonances, however, do not undergo any shift; see the HSQC map in Supporting Information). In addition, we see the intensity loss of the N42 side chain amide around 8 ppm and the slight chemical shift changes of S28 and L40 backbone amides at about 9 ppm. On the other hand, the differences that are seen in the aliphatic region are due to citrate and stabilizing surfactants that occur in the nanoparticle preparations.

NMR Experimental Evidence. One-dimensional ^1H and 2D [^1H , ^{15}N] HSQC NMR experiments have been used to characterize, at amino acid residue level, the interaction between $\beta_2\text{m}$ and gold nanoparticles at various molar ratios. Different samples containing 130 nM of 5 nm AuNP (Sigma-Aldrich) and variable $\beta_2\text{m}$ concentrations ranging from 4 to 36 μM were analyzed.

A general decrease of $\beta_2\text{m}$ signal intensity in ^1H monodimensional experiments when Au nanoparticles were added is highlighted in Figure 8, whereas chemical shifts are only marginally affected.

In fact, the presence of nanoparticles affects the protein signal intensities much more than chemical shifts. The attenuation tends to decrease as the protein concentration increases and arises from exchange average between the free molecule and the species

transiently in contact with the nanoparticle. Due to the slower tumbling of the protein nanoparticle adduct with respect to the free molecule, the resulting larger extent of dipolar broadening propagates to the free species because of fast exchange, thereby attenuating the overall sampled signal. This behavior is consistent with protein–nanoparticle interactions also confirmed by a surface plasmon resonance absorption red shift of 3.4 nm shown in Figure 9.

Similar shifts were reported for hUbc and azurin.²⁶ The comparison of 1D spectra of $\beta_2\text{m}$ alone and with AuNP presence suggests the absence of any significant chemical shift perturbation that is confirmed by the complete cross-peak overlap of HN signals in 2D [^1H , ^{15}N] HSQC maps acquired with and without nanoparticles (results are shown in Figure 2 of Supporting Information).

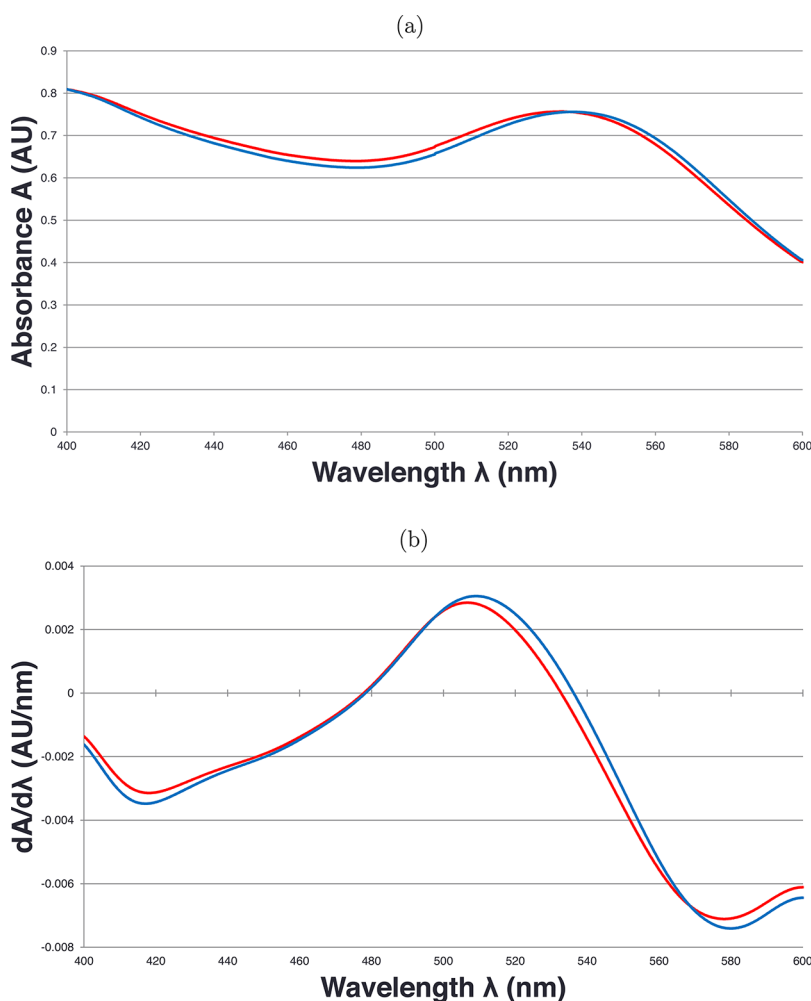


Figure 9. UV–vis spectra of AuNP free and bound to β_2m in red and blue, respectively. AuNP and β_2m are at a concentration of 130 nM and 26 μM . (a) UV–vis spectrum and (b) spectrum derivative highlight the surface plasmon resonance red shift of 3.4 nm.

This is the signature of a conserved protein fold also when the protein interacts with the gold–citrate surface. On the contrary, the analysis of the normalized cross-peak intensities, shown in Figure 10, reveals differential behaviors of the observed HN connectivity signals, suggesting variable dipolar contributions to relaxation for the various amide locations that approach the surface of the AuNPs more closely.

Simple steric consideration, based on the protein modeled as a sphere or with an oblate shape, has led to speculation that 15–25 molecules can be accommodated in a layer surrounding a 5 nm diameter nanoparticle. These estimates are probably in excess because a very close packing is implied but tell us that in the present experimental conditions, even at the lowest tested β_2m concentration, the number of protein molecules largely exceeds the amount required to cover the particle surface. Therefore, the present results reflect the fast exchange between the bound and free state of the protein, in the context of a labile protein–nanoparticle adduct. This, in turn, suggests a weakly bound protein layer surrounding the NPs, also

referred to as soft corona;¹³ even if the corresponding hard corona would be poorly observable by NMR because of an expected rather slow rotational tumbling rate, there are a few elements that make the occurrence of a tightly bound layer of β_2m around the small AuNPs unlikely. First, the size of the NPs is not that large to support a tightly bound first corona layer.¹³ The actual interaction between the citrate-coated surface of the NPs and the protein should be electrostatic, as confirmed by simulation, but the overall protein charge should be around zero or slightly negative, which definitely attenuates the layer tightness. The substantial agreement between simulation and experiment for the NP close approach or contact points on the protein surface suggests that the loosely bound layer of protein molecules we observe experimentally does not establish contacts with any hard corona layer of protein molecules. The experimental differential attenuation pattern, on the other hand, cannot be attributed to the citrate because control experiments (not shown) confirm the absence of any correlation between the pattern observed with citrate-coated

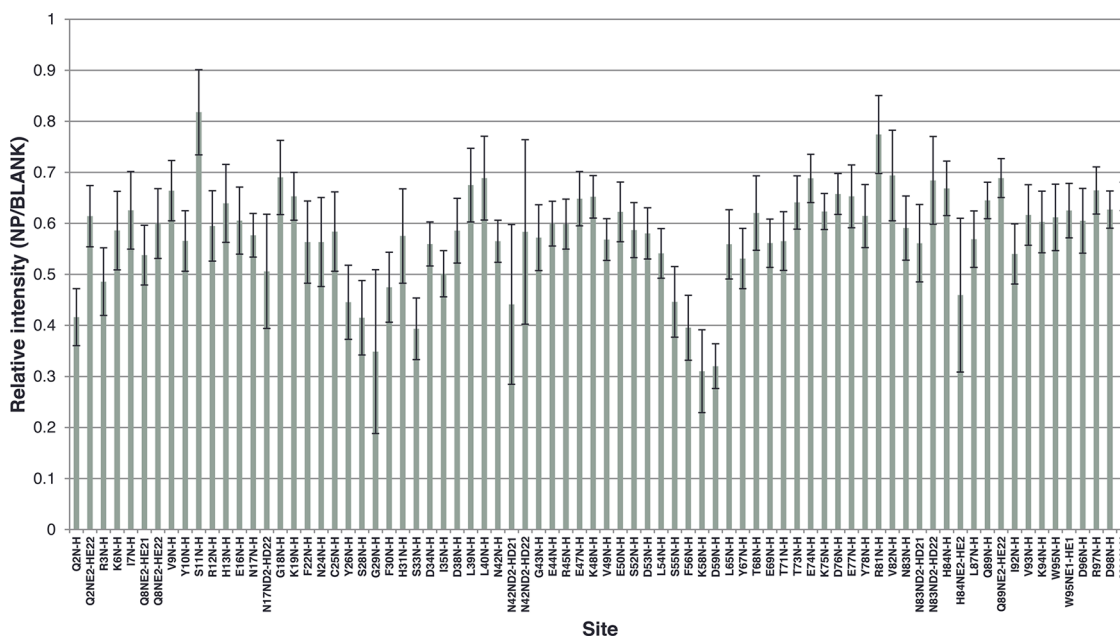


Figure 10. Relative intensities of $\beta_2\text{m}$ HSQC cross-peaks in the free and bound state at a protein concentration of $17 \mu\text{M}$.

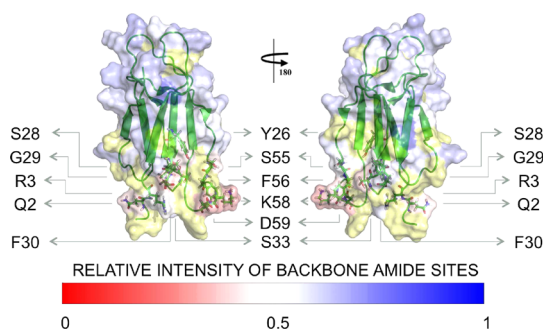


Figure 11. β_2 -microglobulin surface colored according to the relative intensity scale. The residues whose backbone amide sites have less than 0.5 relative intensities are highlighted. Amide residues not measured in the analysis are in yellow.

AuNPs and that obtained with citrate alone. The described weak interaction regime appears to be consistent with the experimentally observed attenuation pattern of the protein signals. The normalized intensities in Figure 10 for the backbone amide peaks obtained from the $26 \mu\text{M}$ sample are highlighted on the $\beta_2\text{m}$ molecular structure in Figure 11 (PDB code 1JNJ) through appropriate color coding.

The picture renders the involvement in the interaction with AuNPs of the N-terminal apical part of the protein, in particular, GLN2 and ARG3 in the N-terminus and LYS58 and ASP59 in the DE loop, in good agreement to complex A of the simulations, as already discussed in Figure 3. In addition, we could also identify other close interaction sites, in the DE loop, SER55 and PHE56 in strand B, and residues TYR26, SER28, GLY29, PHE30, and SER33 in the following BC loop. This interaction pattern is proven to be independent from the experimental protein/nanoparticle molar ratio. Very similar pictures emerged, in fact, when the $\beta_2\text{m}$

concentration was lowered to $4 \mu\text{M}$ with a $\beta_2\text{m}/\text{AuNP}$ ratio of about 30. The same residue involvement was assessed with the addition of LYS6, ASN42, and LEU65. These additional involvements may reflect the less-populated binding modes which are expected to occur from rigid docking (see Supporting Information) and whose occurrence should be more easily observed at low protein concentration excess with respect to AuNPs. To test a long-term effect of AuNP on $\beta_2\text{m}$ stability, we repeatedly acquired HSQC spectra over 4–7 days from sample preparation—and more recently over about a month with an analogous system—without revealing any significant variation (data not shown). This result establishes over macroscopically accessible time frames the conformational stability elements observed in T-REMD analysis.

CONCLUSIONS

In this article, we have presented an extensive set of experimental and computational studies of the interaction between $\beta_2\text{m}$ and citrate-capped gold NPs. We have used atomically detailed simulations at multiple levels of theory, including docking by Brownian dynamics, Poisson–Boltzmann electrostatics, and enhanced atomistic MD. From these simulations, we could provide molecular insights into the $\beta_2\text{m}$ –cit–AuNP interactions that are not directly accessible from experiments. In particular, on the basis of our results on protein–surface docking and implicit solvation modeling, we discussed the nature of the interactions that guide the binding of $\beta_2\text{m}$ to the citrate-capped gold nanoparticle, finding that long-range electrostatic interactions are the leading terms for the encounter complex. In fact, the orientation of the protein relative to the particle surface is determined by

such interactions and is in agreement with the experimental results from NMR spectroscopy. Moreover, the comparison between docking results obtained by mimicking the experimental conditions clearly shows that the adlayer of citrate molecules does remain on the surface of the NP, coexisting with the adsorbed protein, similarly to what was previously shown for other proteins on cit-AuNPs.^{27,58} Both experiments and simulations suggest that the internal rearrangements of the protein induced by the interaction with the charged surface of cit-AuNPs are not able to disrupt the secondary structure of the native protein thus do not lead to unfolded amyloidogenic intermediates. The overall picture is consistent with the small dimensions of the AuNPs and the labile interaction regime that occurs between β_2m and the AuNPs. Our MD results also suggest that the effects

of protonation of HIS31, known to destabilize the protein toward amyloidogenic intermediates, are enhanced by the interaction with the negative surface. Our work also offers a fresh view on the interaction of the protein with biomolecules comprising negative charge arrays.

The results presented here, combined with our previous findings on hydrophobic NPs,⁵⁵ suggest that, by properly balancing the extent of electrostatic and hydrophobic interactions, the NP surface may provide stabilization/destabilization to amyloidogenic proteins as shown in the comparison between nonprotonating and protonating conditions. Therefore, NP-based approaches to treat amyloid pathologies may be definitely conceived once the available ingredients for NP performance are adapted to the properties of the specific protein surface.

METHODOLOGY

Electrostatic Model. The structure of β_2 -microglobulin (PDB code 1JNJ) was preprocessed using PDB code 2PQR⁵⁹ using the CHARMM set of radii and charges. In view of the high negative potential due to the nanoparticle, HIS51 for which a pK_a of 6.6 is predicted using the program BLUUES⁵⁷ was assigned a protonated state. The overall charge of the protein is important for the absolute value of the interaction with the nanoparticle, but the best orientations are less sensitive to it. In the presence of a negatively charged nanoparticle (and consequent local pH lowering), it is expected that the overall charge state of the protein should be close to zero at measured pH 6.5. The structure of β_2 -microglobulin was placed 65 Å distance from the center of the nanoparticle rotated around 100 axes uniformly distributed in the solid angle and identified by the polar angular coordinates θ and ϕ . The rotation angle ψ about the axis was taken from a distribution with probability density

$$\frac{2}{\pi} \sin^2\left(\frac{\psi}{2}\right) = \frac{1}{\pi} (1 - \cos(\psi)) \quad (1)$$

for uniformly sampling the rotation space. The total number of rotations sampled was 800.

NMR Spectroscopy. The interaction between β_2m and AuNP was studied by NMR experiments and UV–vis absorption spectroscopy on samples containing Au nanoparticles at a concentration of 130 nM. NMR experiments were performed at β_2m concentrations of 4, 17, 26, and 36 μM . All samples analyzed were buffered with 25 mM sodium phosphate, pH 6.4, and contained 5% D₂O for lock purposes. NMR experiments were recorded on a Bruker Avance spectrometer operating at 500 MHz (¹H). The 1D ¹H spectra were acquired with 4096 data point, a spectral width of 16 ppm, and 4096 scans. The water suppression was achieved by an excitation sculpting scheme.⁶⁰ The 2D and [¹H,¹⁵N] HSQC spectra were acquired with 1024 128 points in the direct and indirect dimensions, respectively, and 400–1600 scans depending on the sample concentration, over spectral widths of 16 and 37 ppm in the ¹H and ¹⁵N dimensions, respectively. The data were processed with Topspin 2.1 and analyzed with NMRViewJ.⁶¹ The β_2m assignment was based on the file deposited on the Biological Magnetic Resonance Data Bank (accession code 17165). AuNPs, 5 nm in diameter, 0.01% in HAuCl₄ (around 130 nM in NP concentration), were purchased by Sigma-Aldrich (product code G1402) and used without further purification after UV–vis test to verify that no aggregation has taken place.

UV–Vis Absorption Spectroscopy. A spectrum in the range from 400 to 600 nm was acquired with a JASCO UV-530 spectrophotometer

on samples containing Au nanoparticles and β_2m at a concentration of 130 nM and 26 μM , respectively. The experimental conditions for the solutions were the same as those for NMR samples; 1001 points were acquired with a bandwidth of 2.0 nm, a data pitch of 0.2 nm, and a speed of 40 nm/min.

Brownian Dynamics Simulations. Rigid-body docking simulations were carried out using Brownian dynamics techniques with the ProMetCS continuum solvent model for protein–gold surface interactions.⁴⁰ The calculations were performed using the SDA version 6 software.^{62,63} The Au(111) surface was constructed with a surface area of 100 Å × 100 Å and three atomic layers.⁶⁴ The β_2m structure was taken from the NMR solution structure (PDB code 1JNJ). Human β_2m is a 99 residue long, 11.9 kDa protein, with a single disulfide bridge between the two CYS residues of the sequence at positions 25 and 80. The protein folds into the classical β -sandwich motif of the immunoglobulin superfamily, that is, seven antiparallel β -strands (A, B, ..., G), forming two facing sheets (ABED and CFG).⁶⁵

Five thousand BD trajectories were computed starting with the protein positioned randomly with its center at a distance of 70 Å from the surface where the protein–surface interaction energy is negligible. The specified number of docked complexes was extracted directly from the runs and clustered with a clustering algorithm. Experimental salt concentration of 30 mM was included as a nonspecific screening effect on the electrostatic potential of the protein, which was calculated using the APBS program.⁶⁶ The relative translational diffusion coefficient was 0.0123 Å²/ps, and the rotational diffusion coefficient for the protein was 1.36 × 10^{−4} radian²/ps. The simulation time step was set to 0.50 ps. Parameters for the calculation of hydrophobic desolvation energy and forces were set to −0.019 kcal/mol/Å² and for the electrostatic desolvation energy and forces to 1.67 according to ref 67. BD trajectories were generated in a rectangular box (ibox = 1); the dimensions of the (x,y) plane, describing the symmetry of the simulation volume as well as the surface size, were given as input parameters. At each BD step, the protein–surface interaction energy and forces acting on the protein were computed using the implicit solvent ProMetCS force field,⁴⁰ developed and parametrized for protein–gold surface interactions. The energy terms included in ProMetCS have been described in the main text.

Two clustering algorithms were tested and evaluated for this system. These were top-down splitting (hierarchical based on a reference structure) and bottom-up aggregating (single-linkage based on rmsd). The results of docking were preprocessed by translating the protein coordinates parallel to the surface in order to superimpose the protein structures before applying the clustering algorithm. Finally, we applied a single-linkage

clustering method (based on CA atoms, with rmsd = 3.0 Å) for the results given in the article.

Molecular Dynamics Simulations. We have implemented new force field parameters for the citrate anions based on *ab initio* calculations (that take into account the quantum nature of such small chemical species) in a consistent and compatible way with the existing GoIP force field for the protein–AuNP surface interactions.

The regular citrate adlayer on the top of Au(111) was generated with a ratio of the surface gold ion and citrate concentrations suitable to reproduce experimental data.³⁹ The positive atomic charges of the gold surface atoms were set to fit the electronic charges/cm² on the surface of the AuNPs in the electrochemical experiments under aqueous conditions and at physiological pH.³³

For the (i) nonprotonated β_2m , all titratable protein side chains were assigned their standard protonation state at pH 6.8 using the H++ pK calculation program;⁶⁸ (ii) for the protonated protein, additional protonation at HIS31 was performed.

At the beginning of the simulation, the protein was moved away from the surface of the cit-AuNPs by 6 Å, without changing the orientation that resulted from docking. Various tests that we performed showed that the protein in direct contact with the surface is in a kinetically trapped state were only minor relaxation can take place on the time scale of tens of nanoseconds.

For each (i) nonprotonated and (ii) protonated protein, 32 replicas of a rectangular simulation box with dimension of 82 Å × 64 Å × 82 Å, including SPC water molecules, the protein, the citrate adlayer, and the gold surface were built.

Before the solvent was added in the box, the protein was moved away from the surface of the cit-AuNPs by 6 Å, without changing the orientation that resulted from docking. Various tests that we performed showed that the protein in direct contact with the surface is in a kinetically trapped state, where only minor relaxation can take place on the time scale of tens of nanoseconds. All simulations were performed with the Gromacs 4.5.4 package.⁶⁹ GoIP⁶⁴ and OPLS/AA parameters⁷⁰ were used for the surface and the protein, and the SPC/E water model⁷¹ was applied. The bond lengths were constrained with the LINCS algorithm. Surface gold atoms and bulk gold atoms were frozen during all simulations, but gold dipole charges were left free. Periodic boundary conditions and the particle mesh Ewald algorithm were used. A 2 fs integration time step was used.

We performed a total of four independent T-REMD simulations of 20 ns in explicit water for both (i) nonprotonated and (ii) protonated protein in solvent and on the top of the cit-Au(111) surface in the temperature range of 290–320 K.

Trajectories were analyzed in terms of density, temperature, potential energy, and other macroscopic properties with the Gromacs tools (e.g., g_traj, g_rms, g_clusters, etc.). Principal component analysis was also performed using GROMACS, and to compare principal component obtained from independent runs, the covariance matrix was calculated. The eigenvectors and eigenvalues were obtained from diagonalization of the combined covariance matrix, after which coordinates from each independent trajectory were projected along eigenvectors of interest to obtain projection values for given modes.

Conflict of Interest: The authors declare no competing financial interest.

Acknowledgment. Funding from MIUR through PRIN 2012A7LMS3003 is gratefully acknowledged. This work was funded by the Italian Institute of Technology through Platform Computations and Seed project “MOPROSURF—MOdeling PROtein SURface interactions”. The IS CRA staff at CINECA (Bologna, Italy) are acknowledged for computational facilities and technical support. Oak Ridge National Laboratory by the Scientific User Facilities Division, Office of Basic Energy Sciences, U.S. Department of Energy is acknowledged for the supercomputing project CNMS2013-064. Facilities of the National Energy Research Scientific Computing Center (NERSC), which is supported by the Office of Science of the U.S. Department of Energy under Contract No. DE-AC02-05CH11231, are also acknowledged.

Supporting Information Available: Additional figures and table. This material is available free of charge via the Internet at <http://pubs.acs.org>.

Note added in proof: An atomistic simulation of the citrate-gold interface was recently published.⁷²

REFERENCES AND NOTES

- Lundqvist, M.; Stigler, J.; Elia, G.; Lynch, I.; Cedervall, T.; Dawson, K. A. Nanoparticle Size and Surface Properties Determine the Protein Corona with Possible Implications for Biological Impacts. *Proc. Natl. Acad. Sci. U.S.A.* **2008**, *105*, 14265–14270.
- Maiorano, G.; Sabella, S.; Sorce, B.; Brunetti, V.; Malvindi, M. A.; Cingolani, R.; Pompa, P. P. Effects of Cell Culture Media on the Dynamic Formation of Protein–Nanoparticle Complexes and Influence on the Cellular Response. *ACS Nano* **2010**, *4*, 7481–7491.
- Lacerda, S. H. D. P.; Park, J. J.; Meuse, C.; Pristiniski, D.; Becker, M. L.; Karim, A.; Douglas, J. F. Interaction of Gold Nanoparticles with Common Human Blood Proteins. *ACS Nano* **2010**, *4*, 365–379.
- Mahmoudi, M.; Lynch, I.; Ejtehadi, M. R.; Monopoli, M. P.; Bombelli, F. B.; Laurent, S. Protein–Nanoparticle Interactions: Opportunities and Challenges. *Chem. Rev.* **2011**, *111*, 5610–5637.
- Moyano, D. F.; Rotello, V. M. Nano Meets Biology: Structure and Function at the Nanoparticle Interface. *Langmuir* **2011**, *27*, 10376–10385.
- Pelaz, B.; Jaber, S.; de Aberasturi, D. J.; Wulf, V.; Aida, T.; de la Fuente, J. M.; Feldmann, J.; Gaub, H. E.; Josephson, L.; Kagan, C. R.; et al. The State of Nanoparticle-Based Nanoscience and Biotechnology: Progress, Promises, and Challenges. *ACS Nano* **2012**, *6*, 8468–8483.
- Gobin, A.; Lee, M.; Halas, N.; James, W.; Drezek, R.; West, J. L. Near-Infrared Resonant Nanoshells for Combined Optical Imaging and Photothermal Cancer Therapy. *Nano Lett.* **2007**, *7*, 1929–1934.
- Lu, F.; Doane, T. L.; Zhu, J.-J.; Burda, C. Gold Nanoparticles for Diagnostic Sensing and Therapy. *Inorg. Chim. Acta* **2012**, *3006*, 1–12.
- Wright, J. Deliver on a Promise. *Nature* **2013**, *509*, S58–S59.
- Gibbs, B. F.; Yasinska, I. M.; Calzolari, L.; Gilliland, D.; Sumbayev, V. V. Highly Specific Targeting of Human Leukocytes Using Gold Nanoparticle-Based Biologically Active Conjugates. *J. Biomed. Nanotechnol.* **2014**, *10*, 1259–1266.
- Nel, A. E.; Mädler, L.; Velegol, D.; Xia, T.; Hoek, E. M. V.; Somasundaran, P.; Klaessig, F.; Castranova, V.; Thompson, M. Understanding Biophysicochemical Interactions at the Nano-Bio Interface. *Nat. Mater.* **2009**, *8*, 543–557.
- Dawson, K. A.; Salvati, A.; Lynch, I. Nanotoxicology: Nanoparticles Reconstruct Lipids. *Nat. Nanotechnol.* **2009**, *4*, 84–85.
- Rahaman, M.; Laurent, S.; Tawil, N.; Yahia, L.; Mahmoudi, M. *Protein–Nanoparticle Interactions*; Springer-Verlag: Berlin, 2013; Chapter 2, pp 21–44.
- Saptarshi, S. R.; Duschl, A.; Lopara, A. L. Interaction of Nanoparticles with Proteins: Relation to Bio-reactivity of the Nanoparticle. *J. Nanobiotechnol.* **2013**, *11*, 26–37.
- Cabaleiro-Lago, C.; Quinlan-Pluck, F.; Lynch, I.; Dawson, K. A.; Linse, S. Dual Effect of Amino Modified Polystyrene Nanoparticles on Amyloid β Protein Fibrillation. *ACS Chem. Neurosci.* **2010**, *1*, 279–287.
- Lynch, I.; Dawson, K. A. Protein–Nanoparticle Interactions. *Nano Today* **2008**, *3*, 40–47.
- Liao, Y.-H.; Chang, Y.-J.; Yoshiike, Y.; Chang, Y.-C.; Chen, Y.-R. Negatively Charged Gold Nanoparticles Inhibit Alzheimer's Amyloid- β Fibrillization, Induce Fibril Dissociation, and Mitigate Neurotoxicity. *Small* **2012**, *8*, 3631–3639.
- Zhang, M.; Mao, X.; Yu, Y.; Wang, C.-X.; Yang, Y.-L.; Wang, C. Nanomaterials for Reducing Amyloid Cytotoxicity. *Adv. Mater.* **2013**, *25*, 3780–3801.
- Mahmoudi, M.; Kalhor, H. R.; Laurent, S.; Lynch, I. Protein Fibrillation and Nanoparticle Interactions: Opportunities and Challenges. *Nanoscale* **2013**, *5*, 2570–2588.

20. Zaman, M.; Ahmad, E.; Qadeer, A.; Rabbani, G.; Khan, R. H. Nanoparticles in Relation to Peptide and Protein Aggregation. *Int. J. Nanomed.* **2014**, *9*, 899–912.
21. Linse, S.; Cabaleiro-Lago, C.; Xue, W.-F.; Lynch, I.; Lindman, S.; Thulin, E.; Radford, S. E.; Dawson, K. A. Nucleation of Protein Fibrillation by Nanoparticles. *Proc. Natl. Acad. Sci. U.S.A.* **2007**, *104*, 8691–8696.
22. Gejyo, F.; Yamada, T.; Odani, S.; Nakagawa, Y.; Arakawa, M.; Kunitomo, T.; Kataoka, H.; Suzuki, M.; Hirasawa, Y.; Shirahama, T.; et al. A New Form of Amyloid Protein Associated with Hemodialysis Was Identified as β 2-Microglobulin. *Biochem. Biophys. Res. Commun.* **1985**, *129*, 701–706.
23. Relini, A.; Canale, C.; De Stefano, S.; Rolandi, R.; Giorgetti, S.; Stoppini, M.; Rossi, A.; Fogolari, F.; Corazza, A.; Esposito, G.; et al. Collagen Plays an Active Role in the Aggregation of β 2-Microglobulin under Physiopathological Conditions of Dialysis-Related Amyloidosis. *J. Biol. Chem.* **2006**, *281*, 16521–16529.
24. Xia, Y.; Xiong, Y.; Lim, B.; Skrabalak, S. E. Shape-Controlled Synthesis of Metal Nanocrystals: Simple Chemistry Meets Complex Physics? *Angew. Chem., Int. Ed.* **2009**, *48*, 60–103.
25. Sperling, R.; Gil, P.; Zhang, F.; Zanella, M.; Parak, W. J. Biological Applications of Gold Nanoparticles. *Chem. Soc. Rev.* **2008**, *37*, 1896–1908.
26. Calzolari, L.; Franchini, F.; Gilliland, D.; Rossi, F. Protein–Nanoparticle Interaction: Identification of the Gold Nanoparticle Interaction Site. *Nano Lett.* **2010**, *10*, 3101–3105.
27. Brancolini, G.; Kokh, D. B.; Calzolari, L.; Wade, R. C.; Corni, S. Docking of Ubiquitin to Gold Nanoparticles. *ACS Nano* **2012**, *6*, 9863–9878.
28. Sabella, S.; Carney, R. P.; Brunetti, V.; Malvindi, M. A.; Al-Juffali, N.; Vecchio, G.; Janes, S. M.; Bakr, O. M.; Cingolani, R.; Stellacci, F.; et al. A General Mechanism for Intracellular Toxicity of Metal-Containing Nanoparticles. *Nanoscale* **2014**, *6*, 7052–7061.
29. Park, J.-W.; Shumaker-Parry, J. S. Structural Study of Citrate Layers on Gold Nanoparticles: Role of Intermolecular Interactions in Stabilizing Nanoparticles. *J. Am. Chem. Soc.* **2014**, *136*, 1907–1921.
30. Relini, A.; De Stefano, S.; Torrassa, S.; Cavalieri, O.; Rolandi, R.; Gliozzi, A.; Giorgetti, S.; Raimondi, S.; Marchese, L.; Verga, L.; et al. Heparin Strongly Enhances the Formation of β 2-Microglobulin Amyloid Fibrils in the Presence of Type I Collagen. *J. Biol. Chem.* **2008**, *283*, 4912–4920.
31. Colvin, V. M.; Kulinowski, K. M. Nanoparticles as Catalysts for Protein Fibrillation. *Proc. Natl. Acad. Sci. U.S.A.* **2007**, *104*, 8679–8680.
32. Elechiguerra, J. L.; Reyes-Gasga, J.; Yacamán, M. J. The Role of Twinning in Shape Evolution of Anisotropic Noble Metal Nanostructures. *J. Mater. Chem.* **2006**, *16*, 3906–3919.
33. Kunze, J.; Burgess, I.; Nichols, R.; Buess-Herman, I.; Lipkowski, J. Electrochemical Evaluation of Citrate Adsorption on Au(111) and the Stability of Citrate-Reduced Gold Colloids. *J. Electroanal. Chem.* **2007**, *599*, 147–159.
34. Vivek, J. P.; Burgess, I. J. Insight into Chloride Induced Aggregation of DMAP-Monolayer Protected Gold Nanoparticles Using the Thermodynamics of Ideally Polarized Electrodes. *J. Phys. Chem. C* **2008**, *112*, 2872–2880.
35. Scott, H.; Brewer, S. H.; Glomm, W. R.; Marcus, C.; Johnson, M. C.; Magne, K.; Knag, M. K.; Franzen, S. Probing BSA Binding to Citrate-Coated Gold Nanoparticles and Surfaces. *Langmuir* **2005**, *21*, 9303–9307.
36. Lin, Y.; Pan, G.-B.; Su, G.-J.; Fang, X.-H.; Wan, L.-J.; Bai, C.-L. Study of Citrate Adsorbed on the Au(111) Surface by Scanning Probe Microscopy. *Langmuir* **2003**, *19*, 10000–10003.
37. Rostek, A.; Mahl, D.; Epple, M. Chemical Composition of Surface-Functionalized Gold Nanoparticles. *J. Nanopart. Res.* **2011**, *13*, 4809–4814.
38. Wright, L. B.; Rodgera, P. M.; Walsh, T. R. Aqueous Citrate: A First-Principles and Force-Field Molecular Dynamics Study. *RSC Adv.* **2013**, *3*, 16399–16409.
39. Lin, Y.; Pan, G.; Su, G.-J.; Fang, X.-H.; Wan, L.-J.; Bai, C.-L. Study of Citrate Adsorbed on the Au(111) Surface by Scanning Probe Microscopy. *Langmuir* **2003**, *19*, 10000–10003.
40. Kokh, D. B.; Corni, S.; Winn, P. J.; Hoefling, M.; Gottschalk, K. E.; Wade, R. C. ProMetCS: An Atomistic Force Field for Modeling Protein–Metal Surface Interactions in a Continuum Aqueous Solvent. *J. Chem. Theory Comput.* **2010**, *6*, 1753–1768.
41. Gabdoulina, R. R.; Wade, R. C. Effective Charges for Macromolecules in Solvent. *J. Phys. Chem.* **1996**, *100*, 3868–3878.
42. Sugita, Y.; Okamoto, Y. Replica-Exchange Molecular Dynamics Method for Protein Folding. *Chem. Phys. Lett.* **1999**, *314*, 141–151.
43. Hansmann, U. H. E. Parallel Tempering Algorithm for Conformational Studies of Biological Molecules. *Chem. Phys. Lett.* **1997**, *281*, 140–150.
44. Eichner, T.; Kalverda, A. P.; Thompson, G. S.; Homans, S. W.; Radford, S. E. Conformational Conversion during Amyloid Formation at Atomic Resolution. *Mol. Cell* **2011**, *41*, 161–172.
45. Esposito, G.; Ricagno, S.; Corazza, A.; Rennella, E.; Gumral, D.; Mimmi, M.; Betto, E.; Pucillo, C.; Fogolari, F.; Viglino, P.; et al. NMR Spectroscopy Reveals Unexpected Structural Variation at the Protein–Protein Interface in MHC Class I Molecules. *J. Mol. Biol.* **2008**, *378*, 887–897.
46. Eichner, T.; Radford, S. E. A Generic Mechanism of β 2-Microglobulin Amyloid Assembly at Neutral pH Involving a Specific Proline Switch. *J. Mol. Biol.* **2009**, *386*, 1312–1326.
47. Stober, T. S.; Abrams, F. C. Energetics and Mechanism of the Normal-to-Amyloidogenic Isomerization of β 2-Microglobulin: On-the-Fly String Method Calculations. *J. Phys. Chem. B* **2012**, *116*, 9371–9375.
48. Verdone, G.; Corazza, A.; Viglino, P.; Pettirossi, F.; Giorgetti, S.; Mangione, P.; Andreola, A.; Stoppini, M.; Bellotti, V.; Esposito, G. The Solution Structure of Human β 2-Microglobulin Reveals the Prodromes of Its Amyloid Transition. *Protein Sci.* **2002**, *11*, 487–499.
49. Corazza, A.; Pettirossi, F.; Viglino, P.; Verdone, G.; Garcia, J.; Dumy, P.; Giorgetti, S.; Mangione, P.; Raimondi, S.; Stoppini, M.; et al. Properties of Some Variants of Human β 2-Microglobulin and Amyloidogenesis. *J. Biol. Chem.* **2004**, *279*, 9176–9189.
50. Esposito, G.; Corazza, A.; Viglino, P.; Verdone, G.; Pettirossi, F.; Fogolari, F.; Makek, A.; Giorgetti, S.; Mangione, P.; Stoppini, M.; et al. Solution Structure of β 2-Microglobulin and Insights into Fibrillogenesis. *Biochim. Biophys. Acta* **2005**, *1753*, 76–84.
51. Giorgetti, S.; Rossi, A.; Mangione, P.; Raimondi, S.; Marini, S.; Stoppini, M.; Corazza, A.; Viglino, P.; Esposito, G.; Cetta, G.; et al. β 2-Microglobulin Isoforms Display a Heterogeneous Affinity for Type I Collagen. *Protein Sci.* **2005**, *14*, 696–702.
52. Brancolini, G.; Migliore, A.; Corni, S.; Fuentes-Cabrera, M.; Luque, F. J.; Di Felice, R. Dynamical Treatment of Charge Transfer through Duplex Nucleic Acids Containing Modified Adenines. *ACS Nano* **2013**, *7*, 9396–9406.
53. Soliva, R.; Sherer, E.; Luque, F. J.; Laughton, C. A.; Orozco, M. Molecular Dynamics Simulations of PNA3DNA and PNA3RNA Duplexes in Aqueous Solution. *J. Am. Chem. Soc.* **2000**, *122*, 5997–6008.
54. Spector, T. I.; Cheatham, T. E.; Kollman, P. A. Unrestrained Molecular Dynamics of Photodamaged DNA in Aqueous Solution. *J. Am. Chem. Soc.* **1997**, *119*, 7095–7104.
55. Brancolini, G.; Toroz, D.; Corni, S. Can Small Hydrophobic Gold Nanoparticles Inhibit β 2-Microglobulin Fibrillation? *Nanoscale* **2014**, *6*, 7903–7911.
56. Fogolari, F.; Corazza, A.; Varini, N.; Rotter, M.; Gumral, D.; Codutti, L.; Rennella, E.; Viglino, P.; Bellotti, V.; Esposito, G. Molecular Dynamics Simulations of β 2-Microglobulin in Denaturing and Stabilizing Conditions. *Proteins* **2011**, *79*, 986–1001.
57. Fogolari, F.; Corazza, A.; Yarra, V.; Jalaru, A.; Esposito, G. BLUUES: A Program for the Analysis of the Electrostatic Properties of Proteins Based on Generalized Born Radii. *BMC Bioinf.* **2012**, *13*, S18.
58. Brewer, S. H.; Glomm, W. R.; Johnson, M. C.; Knag, M. K.; Franzen, S.; Gold, D. L. M. Probing BSA Binding to

- Citrate-Coated Gold Nanoparticles and Surfaces. *Langmuir* **2005**, *21*, 9303–9307.
59. Dolinsky, T. J.; Czodrowski, P.; Li, H.; Nielsen, J. E.; Jensen, J. H.; Klebe, G.; Baker, N. A. PDB2PQR: Expanding and Upgrading Automated Preparation of Biomolecular Structures for Molecular Simulations. *Nucleic Acids Res.* **2007**, *35*, W522–525.
60. Hwang, T. L.; Shaka, A. J. Water Suppression That Works. Excitation Sculpting Using Arbitrary Waveforms and Pulsed Field Gradients. *J. Magn. Reson., Ser. A* **1995**, *112*, 275–279.
61. Johnson, B. A.; Blevins, R. A. NMR View: A Computer Program for the Visualization and Analysis of NMR Data. *J. Biomol. NMR* **1994**, *4*, 603–614.
62. Gabdouliline, R. R.; Wade, R. C. Simulation of the Diffusional Association of Barnase and Barstar. *Biophys. J.* **1997**, *72*, 1917–1929.
63. www.h-its.org/mcm.
64. Iori, F.; Di Felice, R.; Molinari, E.; Corni, S. GoLP: An Atomistic Force-Field To Describe the Interaction of Proteins with Au(111) Surfaces in Water. *J. Comput. Chem.* **2009**, *30*, 1465–1476.
65. Esposito, G.; Corazza, A.; Bellotti, V. Pathological Self-Aggregation of β_2 -Microglobulin: A Challenge for Protein Biophysics. *Subcell. Biochem.* **2012**, *65*, 1917–1929.
66. Baker, N. A.; Sept, D.; Joseph, S.; Holst, M. J.; McCammon, J. A. Electrostatics of Nanosystems: Application to Microtubules and the Ribosome. *Proc. Natl. Acad. Sci. U.S.A.* **2001**, *98*, 10037–10041.
67. Elcock, A. H.; Gabdouliline, R. R.; Wade, R. C.; McCammon, J. A. Computer Simulation of Protein–Protein Association Kinetics: Acetylcholinesterase-Fasciculin. *J. Mol. Biol.* **1999**, *291*, 149–162.
68. <http://biophysics.cs.vt.edu/H++>.
69. van der Spoel, D.; Lindahl, E.; Hess, B.; Groenhof, G.; Mark, A. E.; Berendsen, H. J. C. GROMACS: Fast, Flexible, and Free. *J. Comput. Chem.* **2005**, *26*, 1701–1718.
70. Jorgensen, W. L.; Maxwell, D. S.; TiradoRives, J. Development and Testing of the OPLS All-Atom Force Field on Conformational Energetics and Properties of Organic Liquids. *J. Am. Chem. Soc.* **1996**, *118*, 11225–11236.
71. Hess, B.; van der Vegt, N. F. Hydration Thermodynamic Properties of Amino Acid Analogues: A Systematic Comparison of Biomolecular Force Fields and Water Models. *J. Phys. Chem. B* **2006**, *110*, 17616–17626.
72. Wright, L. B.; Rodger, P. M.; Walsh, T. R. Structure and Properties of Citrate Overlayers Adsorbed at the Aqueous Au(111) Interface. *Langmuir* **2014**, *30*, 15171–15180.